



Influence of He ion irradiation on the microstructure and hardness of Ni–TiC_{NP} composites

Min Liu¹ · Yong-Feng Yan¹ · Zhen-Bo Zhu² · Lin-Feng Ye² · Ren-Duo Liu² · He-Fei Huang^{2,3}

Received: 2 August 2021 / Revised: 14 September 2021 / Accepted: 15 September 2021 / Published online: 16 November 2021
© The Author(s), under exclusive licence to China Science Publishing & Media Ltd. (Science Press), Shanghai Institute of Applied Physics, the Chinese Academy of Sciences, Chinese Nuclear Society 2021

Abstract In the present study, samples of a titanium carbide nanoparticle-reinforced nickel alloy (Ni–TiC_{NP} composite) were irradiated with 1 MeV He ions at 700 °C. The evolution of He bubbles and nanohardness was characterized using transmission electron microscopy (TEM) and nanoindentation, respectively. TEM images showed that the size and number density of He bubbles in the grains were affected by the He ion fluence. The number density first increased significantly and then decreased with increasing ion dose, while the size exhibited an inverse trend. Moreover, the swelling induced by He bubbles continuously increased with increasing ion dose. He bubbles also formed in the grain boundaries, interior of the TiC nanoparticles, and interfaces between the TiC nanoparticles and Ni matrix. Nanoindentation measurements indicated a decrease in nanohardness after irradiation, which is attributed to the disappearance of intrinsic dislocation lines caused by He ion irradiation.

Keywords Ni–TiC_{NP} composites · He bubbles · Swelling · Irradiation-induced softening

This work was supported by the National Natural Science Foundation of China (Nos. 11705264, 11975304, 12022515, and 12175323).

✉ He-Fei Huang
huanghefei@sinap.ac.cn

¹ Sino-French Institute of Nuclear Engineering and Technology, Sun Yat-Sen University, Zhuhai 519082, China

² Shanghai Institute of Applied Physics, Chinese Academy of Sciences, Shanghai 201800, China

³ School of Nuclear Science and Technology, University of Chinese Academy of Sciences, Beijing 100049, China

1 Introduction

Nuclear power is an important method for achieving carbon neutrality [1]. To avoid the occurrence of nuclear accidents such as the Fukushima accident [2], it is important to develop nuclear reactors with inherent safety. Among the fourth-generation reactors, the molten salt reactor (MSR) is very attractive because it is very safe and reliable [3]. High temperatures, molten salts, and neutron irradiation are the major challenges of the structural materials used in MSRs. Ni-based alloys [4–8] are the most promising structural material because of their good corrosion resistance [9]. However, structural alloys for MSRs will experience neutron irradiation, and He atoms will be generated by nuclear transmutation. He atoms can easily form bubbles in the grains and grain boundaries, resulting in the swelling, hardening, and embrittlement of Ni-based alloys at high temperatures [10–14], which limits their application in MSRs. Many novel Ni-based alloys, such as Ni–W–Cr alloys [15], NiMo dispersion precipitation strengthened (DPS) alloys [16], SiC nanoparticle-reinforced Ni-based composites [17], and other alloys [18], have been developed to improve the operating temperature and irradiation resistance for future application in high-temperature MSRs.

In our previous work [19], TiC nanoparticles were successfully added to pure Ni by ball milling and spark plasma sintering to prepare Ni–TiC_{NP} composites using a powder metallurgy route. As a reinforcement phase, the dispersed TiC nanoparticles effectively enhanced the strength. It was also noticed that the Ni–TiC interfaces may influence the formation of He bubbles. For example, TiC particles can suppress bubble nucleation in W–TiC alloys [20]. Thus, it is important to study the distribution of He

bubbles in Ni–TiC_{NP} composites and their evolution with the He concentration. Ion irradiation effectively introduces neutron irradiation-induced displacement damage and He atoms without inducing radioactivity in alloys. Therefore, in this study, He ion irradiation was performed on Ni–TiC_{NP} composites. Considering that Ni–0.05TiC_{NP} composites ball-milled for 24 h have the maximum strength, they were selected and irradiated with He ions at different ion fluences in this study. The irradiation temperature was 700 °C, which is greater than half the melting temperature ($0.5 T_m$) of the alloy. The effects of He ion irradiation on the microstructure and nanohardness of the Ni–0.05TiC_{NP} composites were studied by transmission electron microscopy (TEM) and nanoindentation.

2 Material and methods

Mixed powders comprising 95% Ni powder and 5% TiC powder were ball-milled for 24 h. Ni–0.05TiC_{NP} alloys were prepared using a spark plasma sintering (SPS) furnace [19]. The average grain size of the Ni–0.05TiC_{NP} alloy was approximately $2.87 \pm 0.45 \mu\text{m}$. They were then cut into thin sheets. The length, width, and height of the sheets were 1, 0.65, and 0.1 cm, respectively. The samples were first mechanically polished. They were then electropolished at 0 °C with a solution of 50% sulfuric acid, 40% glycerin, and 10% deionized water for 10 s. Finally, they were cleaned with acetone, absolute ethyl alcohol, and deionized water.

The samples were then irradiated at 700 °C with 1 MeV He⁺ ions at the Shanghai Institute of Applied Physics, Chinese Academy of Sciences, using a 4 MV Pelletron accelerator. The ion flux for irradiation was approximately 3×10^{12} ions/(cm² s). The He concentration and displacement per atom (dpa) profiles were simulated by the Stopping and Range of Ions in Matter (SRIM) 2013 software using the “Detailed Calculation with Full Damage Cascades” mode [21]. The displacement energies of Ni for the calculation were 40 eV, and Ti and C were ignored because of the small mass fraction (5%) of TiC. As shown in Fig. 1, the He concentration first increased and then decreased with increasing depth. The dpa profiles exhibited a similar trend, and the damage peak was located at 1675 nm. The injection depth of 1 MeV He ions into the Ni–TiC_{NP} composites was ~ 2000 nm. The irradiation fluences were 5×10^{15} , 5×10^{16} , and 1×10^{17} ions/cm², and the peak He concentration and displacement damage are listed in Table 1.

TEM specimens of the irradiated samples were prepared using the focused ion beam (FIB) technique, which was performed at the WinTech Nano-Technology Services Pte., Ltd., Suzhou, using an FEI Helios G4 FIB system. Pt layers

were deposited to protect the surfaces of the irradiated samples. Ga ions at 30 and 5 keV were used to perform the initial milling and final polishing, respectively. TEM observations were performed using an FEI Tecnai G2 F20 S-TWIN microscope at the Shanghai Institute of Applied Physics, Chinese Academy of Sciences. The accelerating voltage was 200 kV. The thickness of the TEM samples was approximately 80 nm, which was estimated using convergent-beam electron diffraction (CBED). TEM images under different modes, including underfocused, overfocused, and two-beam conditions, as well as selected area electron diffraction (SAED) patterns were taken to study the microstructural evolution.

The nanohardness of the irradiated samples was measured using a G200 nanoindenter in the continuous stiffness measurement (CSM) mode. The corresponding loading mode was displacement-controlled, and the strain rate was 0.05 s^{-1} for each test. Twelve indentations were performed for each sample. For each irradiated sample, the nanohardness was tested in the unirradiated and irradiated regions, which were exposed to the same high-temperature annealing.

3 Results and discussion

3.1 He bubble evolution

A cross-sectional transmission electron microscopy (XTEM) image of irradiated sample S1 (5×10^{15} ions/cm²) is displayed in Fig. 2a. Some grain boundaries and dispersed TiC nanoparticles were observed. The SAED pattern in the damage band is shown in the inset of Fig. 2a, indicating that the crystal structure of sample S1 remained unchanged during irradiation. Figure 2b presents a magnified TEM image of the peak damage zone marked by the red box in Fig. 2a. Many white defects were observed, which were identified as He bubbles via through-focus experiments. Figure 2c, d display high-magnification underfocused and overfocused TEM images, respectively, from the other peak implantation zone. It can be seen that the He bubbles in Fig. 2c changed into black dots in the overfocused condition (Fig. 2d).

An XTEM image of sample S2 irradiated at 5×10^{16} ions/cm² is shown in Fig. 3a. The overall He bubble band is shown in Fig. 3b. Compared to sample S1, the density of He bubbles in the damage band of sample S2 increased significantly. However, the size of the bubbles decreased slightly. The average size of the He bubbles in the peak damage region appeared almost unchanged, as shown in Fig. 3c.

Figure 4a shows an XTEM image of sample S3 irradiated at 1×10^{17} ions/cm². The enlarged TEM image of

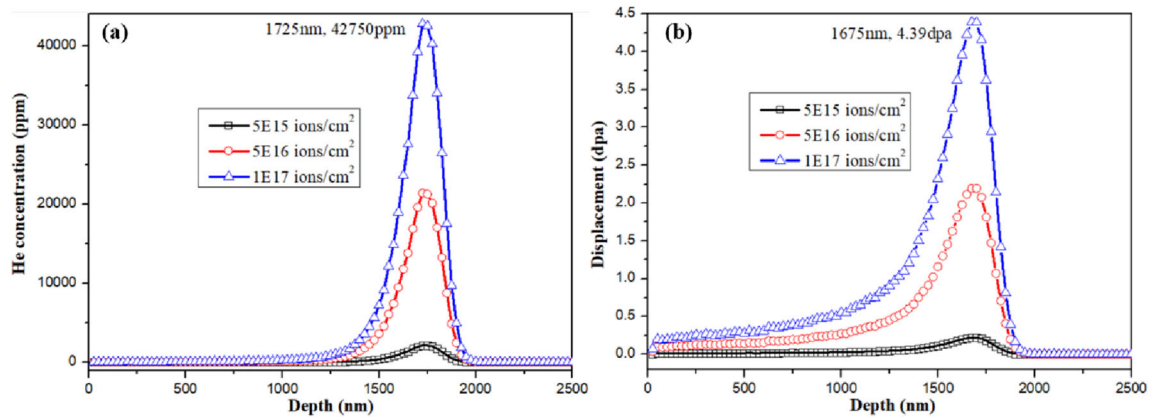
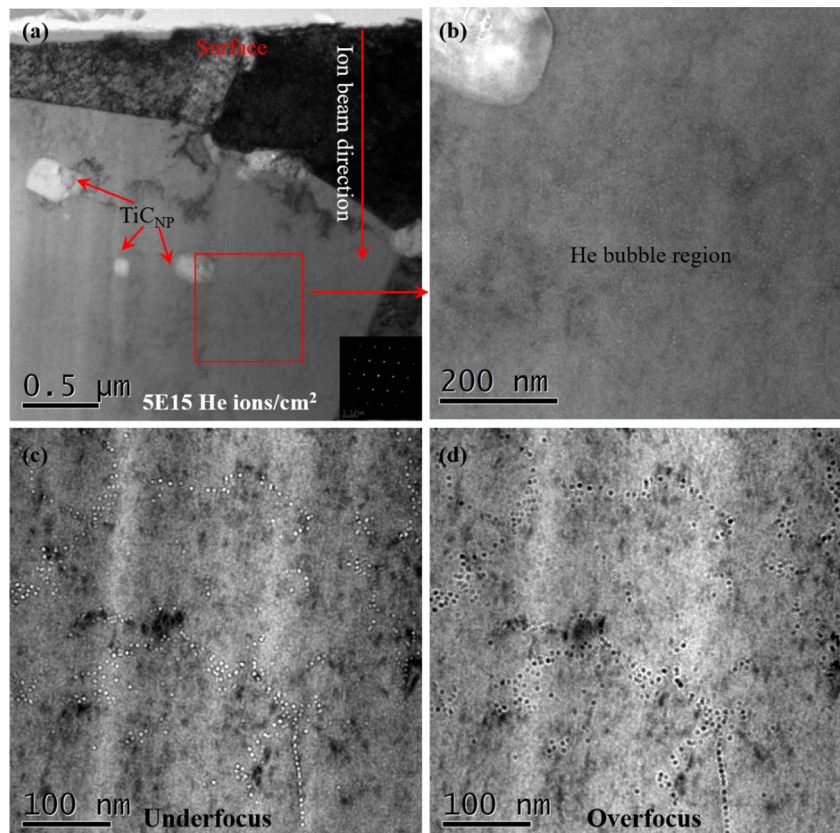


Fig. 1 **a** He concentration and **b** dpa profiles in the Ni-0.05TiC_{NP} composite irradiated by 1 MeV He⁺ calculated by SRIM. The corresponding ion fluences were 5×10^{15} , 5×10^{16} and 1×10^{17} ions/cm²

Table 1 Irradiation conditions, peak He concentration, and displacement damage of Ni–0.05TiC_{NP} samples

Sample	Temperature (°C)	Energy (MeV)	He ion fluence (ions/cm ²)	Peak He concentration (ppm)	Peak damage (dpa)
S1	700	1	5×10^{15}	2137	0.22
S2	700	1	5×10^{16}	21,375	2.20
S3	700	1	1×10^{17}	42,750	4.39

Fig. 2 **a** XTEM image of sample S1 irradiated by 5×10^{15} He ions/cm², the inset displays the SAED pattern of the peak damage zone. **b** The zoomed TEM image of the region marked by the red box. **c** and **d** the underfocus and overfocus TEM images of the peak damage zones



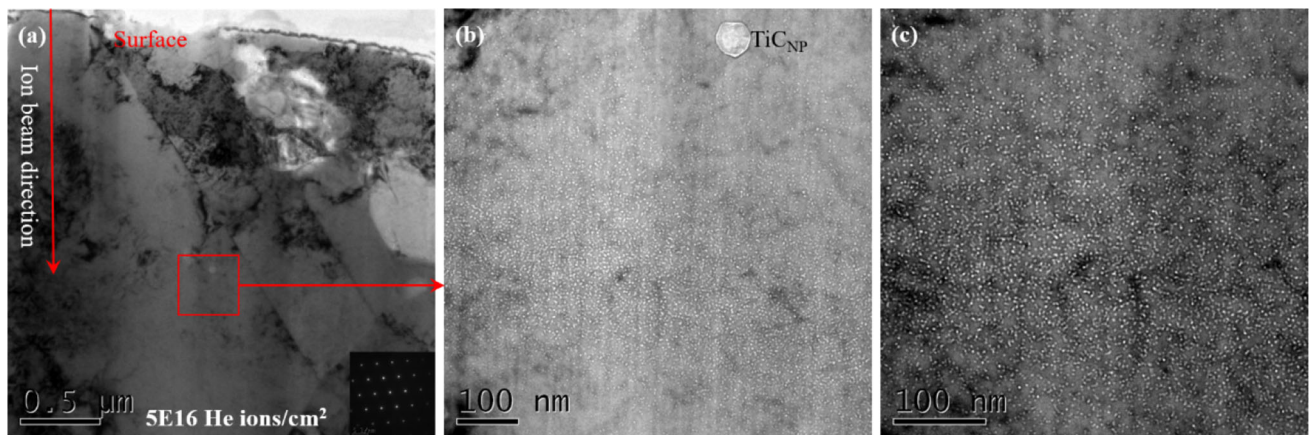
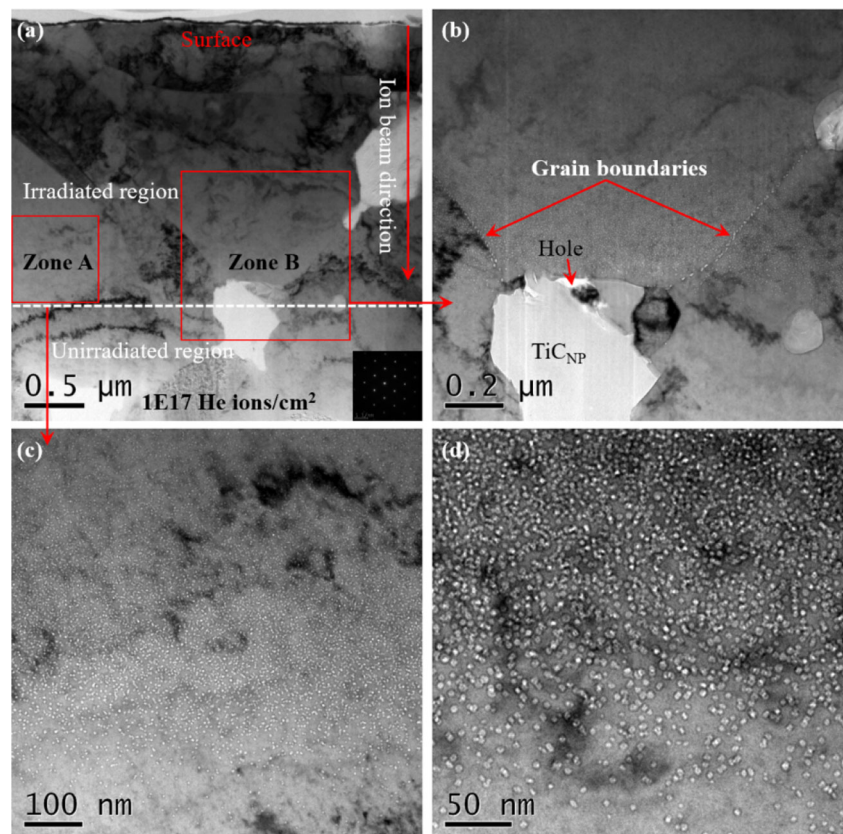


Fig. 3 **a** XTEM image of sample S2 irradiated by 5×10^{16} He ions/cm², the inset displays the SAED pattern of the peak damage zone. **b** The TEM image of He bubble region marked by the red box. **c** Enlarged TEM image in peak damage zone

Fig. 4 **a** XTEM image of the sample S3 irradiated by 1×10^{17} He ions/cm², the SAED pattern of the peak damage zone was displayed in the inset; **b** Amplified TEM image of zone B; **c** and **d** enlarged TEM image of zone A



zone B in sample S3 is shown in Fig. 4b. He bubbles formed at two grain boundaries. Figure 4c displays the He bubble bands in the matrix, which are indicated by red box A. The corresponding high-magnification TEM image near the peak damage region is shown in Fig. 4d. When the depth exceeded the peak damage zone, the density of bubbles decreased, and their size increased.

The He bubbles that formed in the peak damage regions in the Ni matrix of the samples irradiated at different He

ion doses are displayed in Fig. 5 for direct comparison. It can be clearly observed that the density and size of the He bubbles varied with the dose. When the ion fluence was increased from 5×10^{15} to 5×10^{16} ions/cm², the size decreased slightly; however, the bubble density increased significantly. When the fluence was further increased to 1×10^{17} ions/cm², larger bubbles formed, and the density showed a slight reduction.

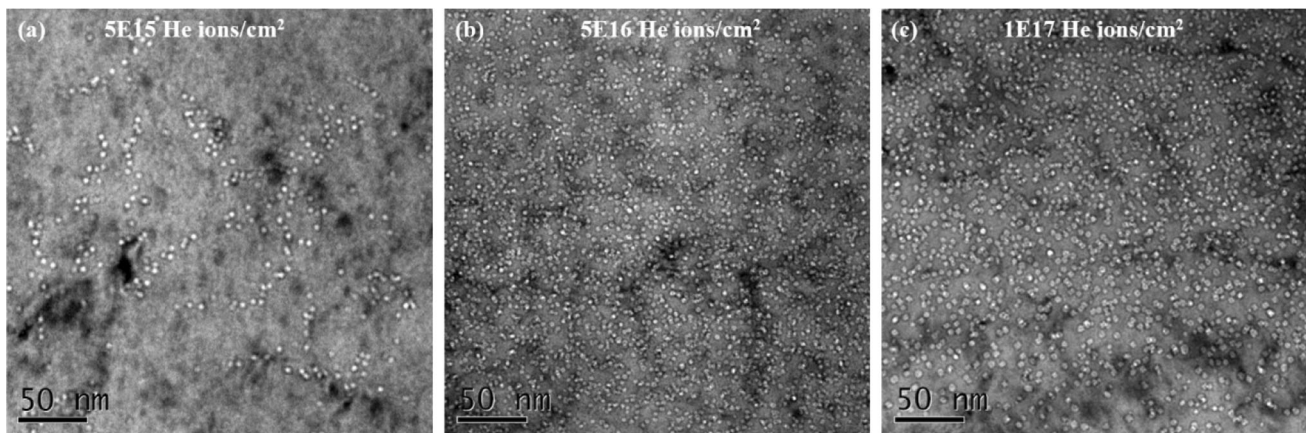
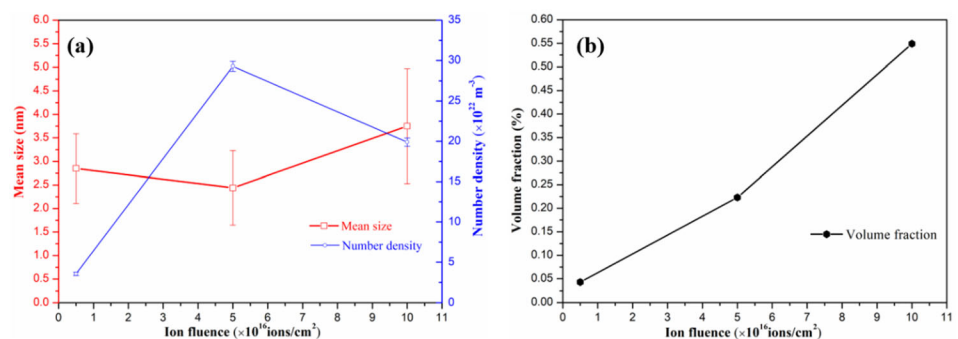


Fig. 5 Bright field TEM images of He bubbles at the peak damage zones of the samples: **a** S1, **b** S2 and **c** S3

Fig. 6 a The mean size and number density and **b** volume fraction of He bubbles in the peak damage regions of samples irradiated to different ion fluences



The number density and mean He bubble size for the three irradiated samples were calculated by the “Nano Measurer” software, as shown in Fig. 6a. The number densities of bubbles in the samples (S1, S2, and S3) were approximately $(3.56 \pm 0.22) \times 10^{22}$, $(29.3 \pm 0.62) \times 10^{22}$, and $(19.9 \pm 0.51) \times 10^{22}$ m⁻³, respectively, and the corresponding mean diameters were approximately 2.85 ± 0.74 , 2.44 ± 0.79 , and 3.75 ± 1.22 nm, respectively. Clearly, the number density and size of He bubbles varied with the ion fluence. It is known that implanted He atoms can aggregate to form He bubbles. Furthermore, the implantation of energetic He ions results in the displacement of Ni atoms, which then collide with other Ni atoms to form displacement cascades. During this process, vacancies and interstitials are generated. In this study, when the dose was low, a low density of He bubbles formed. These bubbles were not equally distributed in the grains. They tended to be connected by a series of lines, which may be related to the pre-existing dislocation lines in the Ni–0.05TiC_{NP} composites. He atoms can become trapped at dislocations to form He bubbles [22]. At a low dose (5×10^{15} ions/cm²), the implanted He atoms would preferentially nucleate at dislocation lines and aggregate to form He bubbles. He atoms can also be trapped by displacement damage-induced

vacancy clusters to form nucleation sites for He bubbles. When the He ion dose was increased to 5×10^{16} ions/cm², more He atoms and vacancies were generated, which could provide considerably more nucleation sites for He bubbles. Therefore, the number density of He bubbles in sample S2 increased significantly. Although the total number of He atoms increased, they were dispersed by He–vacancy complexes and the pre-existing dislocations, which caused the average size to decrease slightly from 2.85 ± 0.74 nm to 2.44 ± 0.79 nm. When the He ion dose was further increased to 1×10^{17} ions/cm², He bubbles became dense, and some bubbles gathered to form large bubbles through the “Migration and Coalescence” (MC) mechanism [9], causing the disappearance of some bubbles and a slight decrease in their number density.

It is widely reported that He bubbles can cause swelling of Ni-based alloys [10, 11, 13, 23, 24]. For example, Lei et al. used atomic force microscopy (AFM) to investigate the swelling of a Ni–Mo–Cr alloy irradiated with 1.2 MeV He ions at 650 °C [10]. They found that a swelling of 2.67% was induced by He bubbles in the irradiated sample (3×10^{17} ions/cm², 6.18 dpa), which was larger than that of Ni irradiated to 13 dpa by Ni ions. The swelling can be calculated using the bubble size and number density [25]:

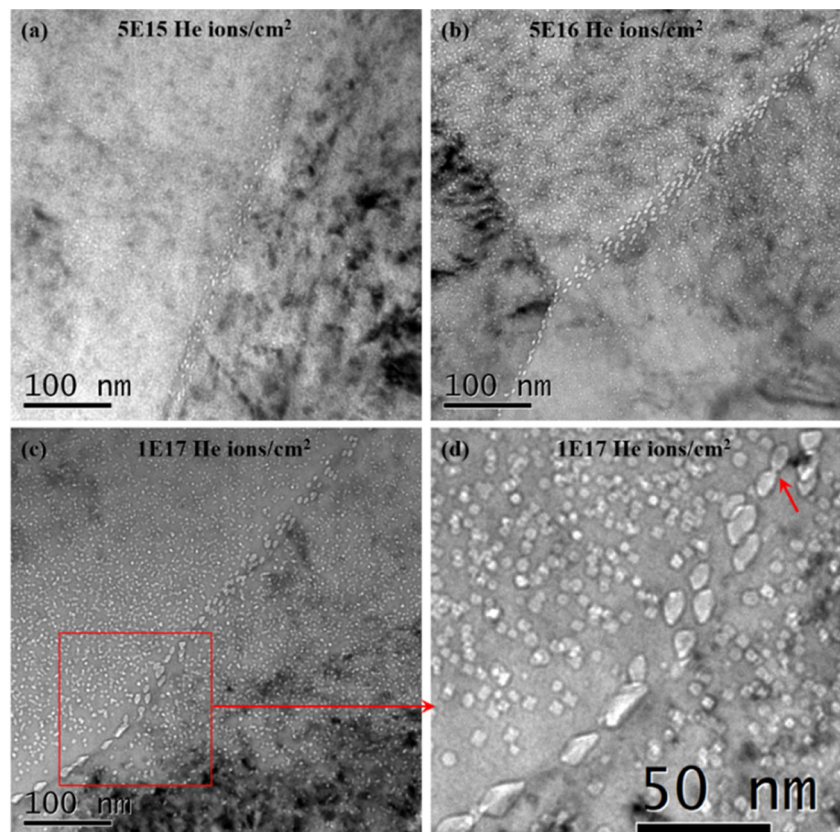
$$\frac{\Delta V}{V} = \frac{4}{3} \pi r^3 N_d, \quad (1)$$

where r is the equivalent radius, and N_d is the number density of the bubbles. The corresponding volume expansion caused by He bubbles in the Ni grain were estimated to be 0.043%, 0.223%, and 0.549% for the samples irradiated at 5×10^{15} , 5×10^{16} , and 1×10^{17} ions/cm². Although the number density tended to saturate at a relatively high dose, the total swelling increased continuously with increasing He ion fluence, as shown in Fig. 6b.

He bubbles formed at the grain boundaries in sample S3, as shown in Fig. 4b. Furthermore, He bubbles were found at the grain boundaries in all the samples irradiated at different doses, as shown in Fig. 7. For sample S1 irradiated at 5×10^{15} ions/cm², the mean He bubble sizes in the grain boundary and matrix were similar (Fig. 7a). As shown in Fig. 7b, c, the bubbles in the grain boundaries were noticeably larger than those in the grains for samples S2 and S3, indicating the preferred formation of He bubbles at the grain boundaries. These He bubbles on the grain boundaries could cause the so-called “He embrittlement” of the alloy, which would degrade the mechanical properties of the structural material in MSRs and should be considered in the design.

Figure 7d shows an enlarged TEM image of He bubbles that formed in the Ni matrix and at the grain boundary in sample S3 irradiated at 1×10^{17} ions/cm². The MC and “Ostwald Ripening” (OR) mechanisms could explain the growth of He bubbles [26, 27]. When the concentration of He atoms is high, the MC mechanism is dominant, which requires the motion and contact of He bubbles. The He ion fluence in sample S3 was 1×10^{17} ions/cm², and the He concentration in the peak region reached 42,750 ppm, which could provide enough He atoms to form a high density of bubbles and enhance the possibility of bubble migration and coalescence. He bubbles at the grain boundary could encounter and contact one another, as shown in Fig. 7d. In particular, the two necked He bubbles indicated by an arrow were in the process of merging. These features indicate that the MC mechanism can explain the growth of He bubbles in this study. For the OR mechanism, He atoms and vacancies released from small dissociated bubbles could be absorbed by large bubbles, and thus larger bubbles could be formed [26, 27]. It has been reported that the OR mechanism is dominant at high temperatures or low concentrations of He atoms [26, 27]. The irradiation temperature (700 °C) was greater than 0.5 T_m of this alloy; therefore, the dissociation of He bubbles was possible. For sample S1 irradiated at a low dose, the OR mechanism may have been dominant. For samples S2

Fig. 7 He bubbles in the grain boundaries in samples **a** S1, **b** S2 and **c** and **d** S3



and S3, the MC and OR mechanisms could both contribute to the growth of He bubbles. Some large ellipsoidal He bubbles elongated along grain boundaries, which resulted from the compressional deformation of bubbles by both sides of the grains during their growth process, were also observed.

It was also noted that the He bubbles in the three irradiated samples had different shapes, which varied with the bubble size. The He bubbles in samples S1 and S2 were relatively small and spherical, as shown in Fig. 5a, b. Both spherical and polygonal He bubbles were observed in sample S3, as shown in Figs. 5c and 7d. The shape of a He bubble is related to its pressure [28]. The internal pressure in a He bubbles is inversely proportional to the bubble size according to the equilibrium bubble pressure equation [28]:

$$P = \frac{2\gamma}{r}, \quad (2)$$

where γ and r are the surface energy of the material and radius of the He bubble, respectively. When the bubble is small, the pressure is relatively large, and spherical He bubbles form easily. When the bubble radius increases, the pressure decreases, resulting in the transformation of He bubbles from stable spherical to polygonal shapes [24].

In the last several years, many types of oxide dispersion-strengthened (ODS) alloys, such as ferritic–martensitic ODS steels [29] and ODS-W alloys [30], have been developed to enhance the irradiation resistance of structural materials in fission and fusion reactors. The dispersed oxide nanoparticles were found to act as He bubble-trapping sites [31, 32]. Similarly, it has been reported that dispersed SiC nanoparticles can inhibit bubble growth and thus reduce the swelling of Ni-based alloys [11], which is attributed to the preferential diffusion of He atoms to the SiC–Ni interface, as revealed by density functional theory (DFT) calculations [11]. However, no He bubbles were observed at the SiC–Ni interfaces in these studies by TEM.

A possible reason is that the size of the He bubbles that formed at these interfaces was too small to be visible. In this study, there were numerous interfaces between the TiC nanoparticles and Ni matrix. In particular, He bubbles were observed at the interfaces between the TiC nanoparticles and Ni matrix, as shown in Fig. 8. Furthermore, it can be seen from Fig. 8a, b that He bubbles also formed in the interior of the TiC nanoparticles, some of which were even larger than the He bubbles in the Ni grains (Fig. 8b). It is proposed that the TiC particles could delay the nucleation and growth of He bubbles in the grains and grain boundaries by confining He atoms to the TiC–Ni interfaces and the interior of the TiC nanoparticles.

3.2 Nanoindentation tests

Nanohardness was measured using nanoindentation to study the influence of He irradiation on the hardness of the samples. It is noted that the high-temperature annealing during irradiation could influence the hardness of the irradiated sample. Thus, to eliminate this interference, the nanohardness of both the unirradiated and irradiated zones of the samples was measured for direct comparison. Figure 9a–c display the variation in the average nanohardness with depth of the unirradiated and irradiated regions in samples S1, S2, and S3, respectively. The corresponding standard deviations are also included. The hardness data for indentation depths less than 100 nm are not shown in Fig. 9 because of inaccuracies in the data due to high uncertainty. The curves demonstrate that the hardness decreases with increasing depth because of the indentation size effect (ISE) [12, 13, 24, 33, 34]. Surprisingly, for each sample, the nanohardness of the irradiated region was lower than that of the unirradiated region, exhibiting an uncommon irradiation-induced softening phenomenon, as shown in Fig. 9a–c. This is quite different from the He irradiation-induced hardening in Ni-based alloys, such as

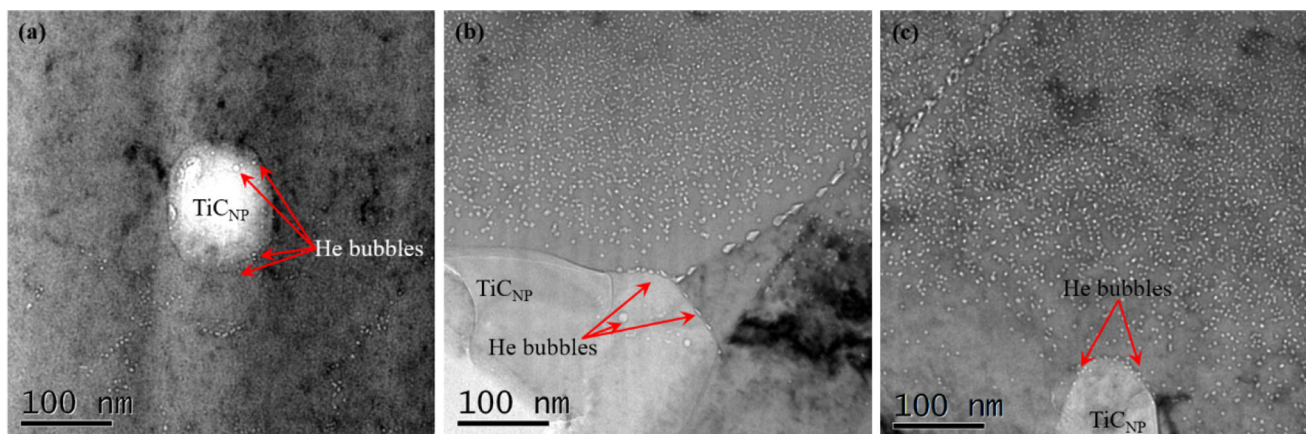


Fig. 8 He bubbles trapped in the TiC_{NP} and the interfaces between TiC_{NP} and Ni matrix in samples: **a** S1, **b** and **c** S3

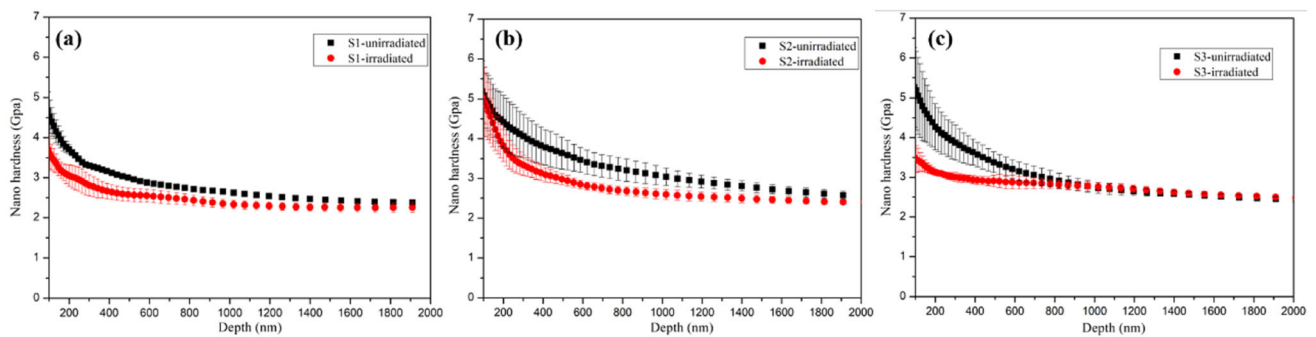


Fig. 9 The average nanoindentation hardness with the depth of unirradiated and irradiated sections of samples **a** S1, **b** S2 and **c** S3

GH3535 [10], Hastelloy N [12], pure Ni, and SiC nanoparticle-reinforced Ni alloys [24]. He ion irradiation-induced hardening of Ni-based alloys was reported in all these studies, and the nanohardness increased with increasing irradiation ion fluence. This type of hardening was attributed to He bubbles and/or dislocation loops. However, although He bubbles formed in this study, the nanohardness of the irradiated samples did not increase but decreased.

To investigate the possible reason for the He irradiation-induced softening, we compared the dislocation microstructure of the unirradiated and irradiated regions of the He-irradiated Ni–TiC_{NP} composite. Figure 10a displays typical bright-field TEM images of the interface between the bubble region and bubble-free region in sample S2 taken under the two-beam condition ($Z = [011]$ and $g = 11\bar{1}$). In the magnified TEM image of the bubble-free region (Fig. 10b), numerous dislocations can be observed. The evolution of these pre-existing dislocation lines can affect the hardness of the material. In the He bubble region (Fig. 10c), the dislocation density decreased, and it appears that some dislocation lines were eliminated by He bubbles.

Similarly, molecular dynamics (MD) simulations indicated that the intrinsic dislocations in single-crystal α -Fe would move under continuous He ion irradiation [35]. The disappearance of intrinsic dislocations in Ni-based alloys induced by Xe ion irradiation was also reported by Chen et al. [36]. We reasonably conclude that the disappearance of pre-existing dislocation lines in the sample resulted from He ion irradiation; however, direct evidence is still missing. In situ TEM observations using He ion irradiation performed within a TEM, which can directly track the growth of He bubbles and the interaction between dislocations and irradiation-induced defects, would be helpful to clarify the interaction between He bubbles and pre-existing dislocation lines in this material [37–39]. When the irradiation dose was low (5×10^{15} ions/cm²), He bubbles were preferentially distributed along a line in the Ni matrix (Figs. 2 and 5), which may have resulted from the interaction between He bubbles and the intrinsic dislocation lines. It was reported that He atoms can be more easily trapped and segregated on dislocations lines [35]. He bubbles formed preferentially along the dislocation lines. During this process, some of the pre-existing dislocation

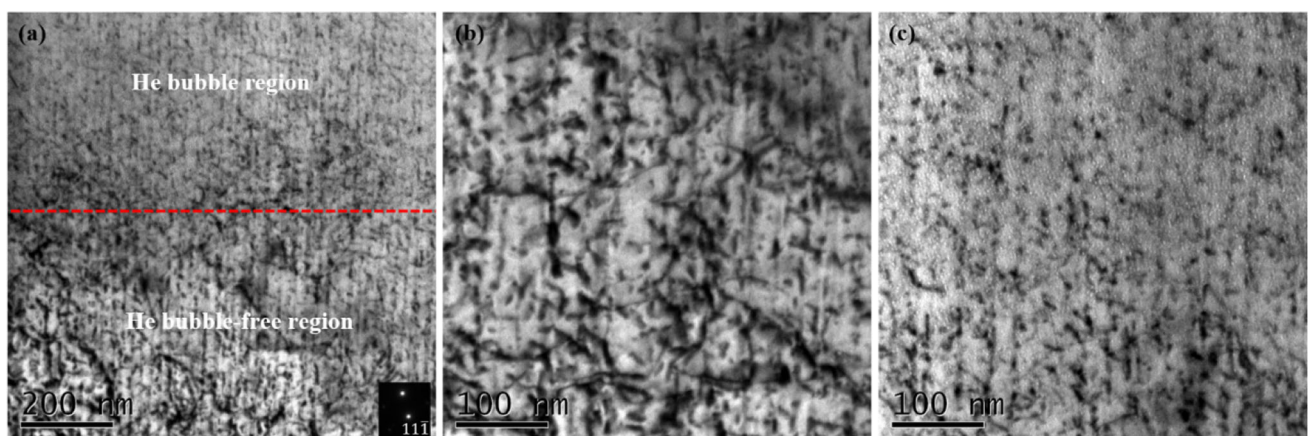


Fig. 10 Bright field TEM images taken under two-beam condition ($g=11\bar{1}$ and $Z = [011]$). **a** Low-magnification TEM image of the interface between He bubble-free zone and bubble zone, **b** the

zoomed TEM image of the bubble-free region and **c** the zoomed TEM image of the bubble region

lines disappeared. Thus, the decrease in hardness may be attributed to the disappearance of the intrinsic dislocations. On the one hand, He bubbles increase the hardness of irradiated samples. On the other hand, the disappearance of the intrinsic dislocations induced by He ion irradiation would decrease the hardness, which exceeds the increment of hardness contributed by He bubbles. Overall, the He ion irradiation induced a softening phenomenon in the Ni–TiC_{NP} composite.

4 Conclusion

In this study, Ni–0.05TiC_{NP} composites ball-milled for 24 h were irradiated with 1 MeV He⁺ ions at 700 °C and 5×10^{15} , 5×10^{16} , and 1×10^{17} ions/cm². TEM was used to investigate the evolution of He bubbles for different ion fluences. Nanoindentation characterizations were performed to reveal the He ion irradiation-induced hardness change. The main conclusions are as follows.

He bubbles formed at the grain boundaries and in the interior of the Ni grain. Ni–TiC interfaces also trapped He atoms in bubbles. At a low dose of 5×10^{15} ions/cm², the density and average size of He bubbles were approximately $3.56 \times 10^{22} \text{ m}^{-3}$ and $2.85 \pm 0.74 \text{ nm}$, respectively. He bubbles tended to be distributed along lines, which may have resulted from preferential absorption by the intrinsic dislocation lines. When the dose was increased to 5×10^{16} ions/cm², the bubble density increased significantly to $2.93 \times 10^{23} \text{ m}^{-3}$, while the average size decreased to $2.44 \pm 0.79 \text{ nm}$. When the dose was further increased to 1×10^{17} ions/cm², the mean size of He bubbles increased to $3.75 \pm 1.22 \text{ nm}$, and the number density showed a minor decrease to $1.99 \times 10^{23} \text{ m}^{-3}$. The corresponding volume expansions induced by He bubbles were calculated to be 0.043%, 0.223%, and 0.549%, indicating increased swelling with increasing irradiation fluence. Some intrinsic dislocation lines were removed by He ion irradiation, resulting in the softening of the Ni–0.05TiC_{NP} composites after He ion irradiation.

Author contributions All authors contributed to the study conception and design. Material preparation, data collection and analysis were performed by Min Liu, Yong-Feng Yan, Zhen-Bo Zhu and He-Fei Huang. The first draft of the manuscript was written by Min Liu and He-Fei Huang commented on previous versions of the manuscript. All authors read and approved the final manuscript.

References

- J.M. Chen, Carbon neutrality: toward a sustainable future. *Innov.* **2**(3), 100127 (2021). <https://doi.org/10.1016/j.xinn.2021.100127>
- G. Chen, Q. Wang, X. Chu, Accelerated spread of Fukushima's waste water by ocean circulation. *Innov.* **2**(2), 100119 (2021). <https://doi.org/10.1016/j.xinn.2021.100119>
- M.W. Rosenthal, P.N. Haubenreich, R.B. Briggs, *The Development Status of Molten-Salt Breeder Reactors. ORNL-4812* (Oak Ridge National Lab, USA, 1972), pp. 195–218
- Y. Zou, X. Wang, P. Lyu et al., Microstructural characteristics of pure nickel foils under argon ion irradiation. *Nucl. Tech.* **44**(8), 080203 (2021). <https://doi.org/10.11889/j.0253-3219.2021.hjs.44.080203> (in Chinese)
- H.E. McCoy, *Status of Materials Development for Molten Salt Reactors. ORNL-TM-5920* (Oak Ridge National Lab, USA, 1978), pp. 1–30
- C.-T. Fu, W. Yinling, X.-W. Chu et al., Grain boundary engineering for control of tellurium diffusion in GH3535 alloy. *J. Nucl. Mater.* **497**, 76–83 (2017). <https://doi.org/10.1016/j.jnucmat.2017.10.052>
- G. Lei, S. Yang, R. Liu et al., The effect of He bubbles on the corrosion properties of nickel-based alloy in molten salt environment. *Nucl. Tech.* **42**(4), 040602 (2019). <https://doi.org/10.11889/j.0253-3219.2019.hjs.42.040602> (in Chinese)
- H.-S. Bao, Z.-H. Gong, Z.-Z. Chen et al., Evolution of precipitates in Ni–Co–Cr–W–Mo superalloys with different tungsten contents. *Rare Met.* **39**(6), 716–724 (2020). <https://doi.org/10.1007/s12598-020-01400-w>
- M. Liu, J. Hou, F. Han et al., Effects of He ion irradiation on the corrosion performance of alloy GH3535 welded joint in molten FLiNaK. *Corros. Sci.* **146**, 172–178 (2019). <https://doi.org/10.1016/j.corsci.2018.10.038>
- G. Lei, R. Xie, H. Huang et al., The effect of He bubbles on the swelling and hardening of UNS N10003 alloy. *J. Alloys Comp.* **746**, 153–158 (2018). <https://doi.org/10.1016/j.jallcom.2018.02.291>
- H.F. Huang, W. Zhang, M. De Los Reyes et al., Mitigation of He embrittlement and swelling in nickel by dispersed SiC nanoparticles. *Mater. Des.* **90**, 359–363 (2016). <https://doi.org/10.1016/j.matdes.2015.10.147>
- Z. Zhu, H. Huang, J. Liu et al., Helium-induced damage behavior in high temperature nickel-based alloys with different chemical composition. *J. Nucl. Mater.* **541**, 152419 (2020). <https://doi.org/10.1016/j.jnucmat.2020.152419>
- Z. Zhu, H. Huang, O. Muránsky et al., On the irradiation tolerance of nano-grained Ni–Mo–Cr alloy: 1 MeV He⁺ irradiation experiment. *J. Nucl. Mater.* **544**, 152694 (2021). <https://doi.org/10.1016/j.jnucmat.2020.152694>
- Fluoride-salt-cooled high temperature reactor (FHR) materials, fuels and components white paper. UCBTH-12-003. pp 1–163 (2013)
- S. Liu, X.-X. Ye, L. Jiang et al., Effect of tungsten content on the microstructure and tensile properties of Ni–xW–6Cr alloys. *Mater. Sci. Eng. A* **655**, 269–276 (2016). <https://doi.org/10.1016/j.msea.2016.01.010>
- C. Yang, T. Wei, G. Zhu et al., Synergistic effect of Mo₂C micro-particles and SiC nanoparticles on irradiation-induced hardening in dispersion-precipitation strengthened NiMo alloys. *Scr. Mater.* **189**, 1–6 (2020). <https://doi.org/10.1016/j.scriptamat.2020.07.058>
- C. Yang, H.-F. Huang, M. De Los Reyes et al., Microstructures and tensile properties of ultrafine-grained Ni–(1–3.5) wt% SiCNP composites prepared by a powder metallurgy route. *Acta. Metall. Sin. (Engl. Lett.)* **28**(7), 809–816 (2015). <https://doi.org/10.1007/s40195-015-0261-5>
- Y. Li, J. Li, C. Fu et al., Damage characteristics of selective laser melted 304L stainless steel under Xe ion irradiation. *Nucl. Tech.* **44**(7), 9–16 (2021). <https://doi.org/10.11889/j.0253-3219.2021.hjs.44.080203> (in Chinese)

19. X. Zhou, H. Huang, R. Xie et al., The key role of ball milling time in the microstructure and mechanical property of Ni-TiCNP composites. *J. Mater. Eng. Perform.* **25**(12), 5280–5288 (2016). <https://doi.org/10.1007/s11665-016-2403-y>
20. Q. Xu, H.Y. Chen, L.M. Luo et al., Microstructural evolution in W-1%TiC alloy irradiated He ions at high temperatures. *Tungsten* **1**(3), 229–235 (2019). <https://doi.org/10.1007/s42864-019-00026-5>
21. J.F. Ziegler, M.D. Ziegler, J.P. Biersack, SRIM—the stopping and range of ions in matter (2010). *Nucl. Instrum. Methods B* **268**(11), 1818–1823 (2010). <https://doi.org/10.1016/j.nimb.2010.02.091>
22. W. Kesternich, Helium trapping at dislocations, precipitates and grain boundaries. *Radiat. Eff.* **78**(1–4), 261–273 (1983). <https://doi.org/10.1080/00337578308207376>
23. A. Liu, H. Huang, J. Liu et al., Improvement of helium swelling resistance of nickel-based alloy via proper SiCNP dispersion. *Mater. Today Commun.* **26**, 102011 (2021). <https://doi.org/10.1016/j.mtcomm.2021.102011>
24. X.L. Zhou, H.F. Huang, R. Xie et al., Helium ion irradiation behavior of Ni-1wt.%SiCNP composite and the effect of ion flux. *J. Nucl. Mater.* **467**, 848–854 (2015). <https://doi.org/10.1016/j.jnucmat.2015.11.004>
25. L.K. Mansur, Theory and experimental background on dimensional changes in irradiated alloys. *J. Nucl. Mater.* **216**, 97–123 (1994). [https://doi.org/10.1016/0022-3115\(94\)90009-4](https://doi.org/10.1016/0022-3115(94)90009-4)
26. J. Gao, H. Huang, X. Liu et al., A special coarsening mechanism for intergranular helium bubbles upon heating: a combined experimental and numerical study. *Scr. Mater.* **147**, 93–97 (2018). <https://doi.org/10.1016/j.scriptamat.2018.01.006>
27. J. Gao, L. Bao, H. Huang et al., Evolution law of helium bubbles in hastelloy N alloy on post-irradiation annealing conditions. *Materials* **9**(10), 832 (2016). <https://doi.org/10.3390/ma9100832>
28. H. Trinkaus, B.N. Singh, Helium accumulation in metals during irradiation—where do we stand? *J. Nucl. Mater.* **323**(2), 229–242 (2003). <https://doi.org/10.1016/j.jnucmat.2003.09.001>
29. M. Klimenkov, R. Lindau, U. Jäntschi et al., Effect of irradiation temperature on microstructure of ferritic-martensitic ODS steel. *J. Nucl. Mater.* **493**, 426–435 (2017). <https://doi.org/10.1016/j.jnucmat.2017.06.024>
30. L.M. Luo, Z.H. Zhao, G. Yao et al., Recent progress on preparation routes and performance evaluation of ODS/CDS-W alloys for plasma facing materials in fusion devices. *J. Nucl. Mater.* **548**, 152857 (2021). <https://doi.org/10.1016/j.jnucmat.2021.152857>
31. J. Chen, P. Jung, W. Höffelner et al., Dislocation loops and bubbles in oxide dispersion strengthened ferritic steel after helium implantation under stress. *Acta Mater.* **56**(2), 250–258 (2008). <https://doi.org/10.1016/j.actamat.2007.09.016>
32. A. Hasegawa, M. Ejiri, S. Nogami et al., Effects of helium on ductile-brittle transition behavior of reduced-activation ferritic steels after high-concentration helium implantation at high temperature. *J. Nucl. Mater.* **386–388**, 241–244 (2009). <https://doi.org/10.1016/j.jnucmat.2008.12.102>
33. W.D. Nix, H. Gao, Indentation size effects in crystalline materials: a law for strain gradient plasticity. *J. Mech. Phys. Solids* **46**(3), 411–425 (1998). [https://doi.org/10.1016/S0022-5096\(97\)00086-0](https://doi.org/10.1016/S0022-5096(97)00086-0)
34. G.M. Pharr, E.G. Herbert, Y. Gao, The indentation size effect: a critical examination of experimental observations and mechanistic interpretations. *Ann. Rev. Mater. Res.* **40**(1), 271–292 (2010). <https://doi.org/10.1146/annurev-matsci-070909-104456>
35. J. Wang, Z. Ma, C. Liu et al., Helium bubble evolution and deformation of single crystal α -Fe. *J. Mater. Sci.* **54**(2), 1785–1796 (2019). <https://doi.org/10.1007/s10853-018-2915-y>
36. H.C. Chen, D.H. Li, R.D. Lui et al., Ion irradiation induced disappearance of dislocations in a nickel-based alloy. *Nucl. Instrum. Methods Phys. Res. Sect. B* **377**, 94–98 (2016). <https://doi.org/10.1016/j.nimb.2016.04.030>
37. Q. Han, Y. Li, G. Ran et al., In-situ TEM observation of the evolution of helium bubbles & dislocation loops and their interaction in Pd during He⁺ irradiation. *J. Mater. Sci. Technol.* **87**, 108–119 (2021). <https://doi.org/10.1016/j.jmst.2021.01.069>
38. Y. Li, G. Ran, Y. Guo et al., The evolution of dislocation loop and its interaction with pre-existing dislocation in He⁺-irradiated molybdenum: in-situ TEM observation and molecular dynamics simulation. *Acta Mater.* **201**, 462–476 (2020). <https://doi.org/10.1016/j.actamat.2020.10.022>
39. Y. Li, L. Wang, G. Ran et al., In-situ TEM investigation of 30 keV He⁺ irradiated tungsten: Effects of temperature, fluence, and sample thickness on dislocation loop evolution. *Acta Mater.* **206**, 116618 (2021). <https://doi.org/10.1016/j.actamat.2020.116618>